Monthly Notices of the ROYAL ASTRONOMICAL SOCIETY

MNRAS **522,** 4728–4739 (2023) https://doi.org/10.1093/mnras/stad1278
Advance Access publication 2023 April 29

Ammonia masers towards G 358.931−0.030

T. P. McCarthy [1★] S. L. Breen [2] J. F. Kaczmarek,[3,4] X. Chen,[5,6] S. Parfenov,[7] A. M. Sobolev [7] S. P. Ellingsen [1] R. A. Burns [8] G. C. MacLeod,[9,10] K. Sugiyama,[11] A. L. Brierley[12] and S. P. van den Heever [10]

[1]*School of Natural Sciences, University of Tasmania, Private Bag 37, Hobart, Tasmania 7001, Australia*
[2]*SKA Observatory, Jodrell Bank, Macclesfield SK11 9FT, UK*
[3]*CSIRO Astronomy and Space Science, Australia Telescope National Facility, Box 76, Epping, NSW 1710, Australia*
[4]*Dominion Radio Astrophysical Observatory, National Research Council of Canada, Box 248, Penticton, BC V2A 6J9, Canada*
[5]*Center for Astrophysics, Guangzhou University, Guangzhou 510006, China*
[6]*Shanghai Astronomical Observatory, Chinese Academy of Sciences, Shanghai 200030, China*
[7]*Astronomical Observatory, Ural Federal University, 19 Mira Street, 620002 Ekaterinburg, Russia*
[8]*Department of Science, National Astronomical Observatory of Japan, 2-21-1 Osawa, Mitaka, Tokyo 181-8588, Japan*
[9]*Department of Physical Sciences, The Open University of Tanzania, PO Box 23409, Dar es Salaam, Tanzania*
[10]*SARAO, Hartebeesthoek Radio Astronomy Observatory, PO Box 443, Krugersdorp 1741, South Africa*
[11]*National Astronomical Research Institute of Thailand (Public Organization), 260 Moo 4, T. Donkaew, A. Maerim, Chiangmai 50180, Thailand*
[12]*Crompton House , Shaw, Oldham OL2 7HS, UK*

Accepted 2023 April 24. Received 2023 April 17; in original form 2022 December 15

ABSTRACT

We report the detection of ammonia masers in the non-metastable (6, 3), (7, 5), and (6, 5) transitions; the latter being the first unambiguous maser detection of that transition ever made. Our observations include the first very long baseline interferometry detection of ammonia maser emission, which allowed effective constraining of the (6, 5) maser brightness temperature. The masers were detected towards G 358.931−0.030, a site of 6.7-GHz class II methanol maser emission that was recently reported to be undergoing a period of flaring activity. These ammonia masers appear to be flaring contemporaneously with the class II methanol masers during the accretion burst event of G 358.931−0.030. This newly detected site of ammonia maser emission is only the 12th such site discovered in the Milky Way. We also report the results of an investigation into the maser pumping conditions, for all three detected masing transitions, through radiative transfer calculations constrained by our observational data. These calculations support the hypothesis that the ammonia (6, 5) maser transition is excited through high colour temperature infrared emission, with the (6, 5) and (7, 5) transition line ratio implying dust temperatures >400 K. Additionally, we detect significant linearly polarized emission from the ammonia (6, 3) maser line. Alongside our observational and radiative transfer calculation results, we also report newly derived rest frequencies for the ammonia (6, 3) and (6, 5) transitions.

Key words: masers – stars: formation – ISM: individual objects: G 358.931−0.030 – ISM: molecules – radio lines: ISM.

1 INTRODUCTION

Ammonia masers have now been detected in at least 32 metastable ($J = K$) and non-metastable ($J > K$) transitions, plus a further 2 isotopic ammonia transitions. The first detections of probable weak masers in the (3, 3) line were reported towards W33 and DR 21(OH) (Wilson, Batrla & Pauls 1982; Guilloteau et al. 1983). The unambiguous detection of non-metastable ammonia transitions was made soon after the (9, 6) transition, initially serendipitously during observations targeting NH_2CCH. Subsequent observations detected (9, 6) masers towards W51, W49, DR 21(OH), and NGC 7538 as well as a (6, 3) maser towards W51 (Madden et al. 1986). Detailed ammonia studies of W51 followed, quickly revealing additional ammonia masers in the (7, 5), (11, 9), (5, 4), and (9, 8) transitions [Mauersberger, Henkel & Wilson 1987; Wilson & Henkel 1988; (10, 8) was also considered a probable maser detection but was not confirmed in later observations by Henkel et al. (2013)], in the (3, 3) transition (Zhang & Ho 1995), and then in the (6, 2), (5, 3), (7, 4), (8, 5), (6, 6), (7, 6), (8, 6), (7, 7), (9, 7) (10, 7), (9, 9), (10, 9), and (12, 12) transitions (Henkel et al. 2013). NGC 7538 also proved to be a prominent site of ammonia maser emission with further studies revealing (10, 6), (10, 8), and (9, 8) masers (Hoffman & Seojin Kim 2011a, b; Hoffman 2012; Hoffman & Joyce 2014), as well as $^{15}NH_3$ masers in the (3, 3) and (4, 3) transitions (Mauersberger, Wilson & Henkel 1986; Johnston et al. 1989; Schilke, Walmsley & Mauersberger 1991). Ammonia (3, 3) masers have also subsequently been detected towards DR 21(OH) (Mangum & Wootten 1994).

Since the early detections, only a handful of further ammonia maser sites have been discovered: NGC 6334 in the (11, 9), (8, 6), (7, 6), (9, 9), (10, 9) (Walsh et al. 2007), (6, 6) (Beuther et al. 2007), and (3, 3) (Kraemer & Jackson 1995) transitions; Sgr B2 in the (2, 2) (Mills et al. 2018), (9, 3), (9, 4), (8, 3), (9, 5), (8, 4), (7, 3), (6, 1), and (6, 4) transitions (Mei et al. 2020); IRAS20126+4104 in (3,

★ E-mail: tiegem@utas.edu.au

Table 1. Details of the primary interferometric ammonia observations, including telescope, array configuration (when the full array was unavailable, the antennas used are given in parentheses), the minimum and maximum baseline lengths, the observation bandwidths used to cover target spectral lines (multiple values indicate that different bandwidths were used for different zoom bands), frequency resolution, phase calibrator used, the total time of the observations, and the total integration time.

Telescope	Epoch DOY	Array	Min, max baseline (m)	BW (MHz)	Res. (kHz)	Phase calibrator	Total time (h)	Int. time (h)
ATCA	064	H214 (3, 4, 5)	82, 240	64	32	B1741−312	4	0.8
ATCA	084	6A	336, 5938	3.5	0.5	B1714−336	4.75	3
VLA	094	B	210, 11 100	4	8	J1744−3116	1.5	0.5
ATCA	096	H75	30, 89	2, 2.5, 3	0.5	B1714−336	6	3.6
ATCA	101	750C	45, 5020	2	0.5	B1714−336	5.5	2.4

3) (Zhang et al. 1999); G 5.89−0.39 in (3, 3) (Hunter et al. 2008); G 9.62+0.19 in (5, 5) (Hofner et al. 1994); G 23.33−0.30 in (3, 3) (Walsh et al. 2011); and G 19.61−0.23 in (11, 9) and (8, 6) (Walsh et al. 2011).

The remarkably small number of ammonia maser sites is despite the extensive, 100-deg^2 survey of the southern Galactic plane for ammonia lines in the (8, 6), (9, 7), (7, 5), (11, 9), (4, 1), (1, 1), (2, 2), (3, 3), (6, 6), and (9, 9) transitions as part of H_2O Southern Galactic Plane Survey (HOPS; Walsh et al. 2011). HOPS has a modest detection limit (with typical 3σ values of between 3–6 Jy) but provides evidence that strong ammonia masers in these transitions are rare.

High spatial resolution observations have revealed the close spatial coincidence between the detected masers and regions of shocks, often found at the interface of molecular outflows with the surrounding environment (e.g. Kraemer & Jackson 1995; Zhang & Ho 1995). The pumping of both metastable and non-metastable ammonia lines is still poorly understood. Currently, the best model for non-metastable maser population inversion is based on vibrational excitation via 10 μm infrared radiation (Brown & Cragg 1991). This pumping mechanism is further supported by observation of maser pairs in the K ladders for ammonia transitions (i.e. J and $J + 1$ for the same K value) by Henkel et al. (2013) towards W51-IRS2. Variability studies of the ammonia maser lines in W51 revealed moderate levels of temporal intensity changes and further that the (9, 6) maser line remained stronger than the (7, 5) and (6, 3) lines (Wilson & Henkel 1988). In other monitoring observations, no obvious temporal variability was identified (Hoffman & Seojin Kim 2011b).

Here, we present a series of ammonia observations, including a number of metastable and non-metastable transitions, towards the location of a 6.7-GHz class II methanol maser, G 358.931−0.030, discovered in the Methanol Multibeam survey (Caswell et al. 2010). The observations were conducted during a period of 6.7-GHz methanol maser flaring activity that was identified by a global cooperative maser monitoring organisation called 'M2O' and first reported by Sugiyama et al. (2019). This flaring event has been attributed to an accretion burst event from the high-mass protostar associated with these masers (Burns et al. 2020; Stecklum et al. 2021). The flaring 6.7-GHz methanol maser has provided an interesting site for multiwavelength follow-up observations, including searches for new maser transitions, subsequent very long baseline interferometry (VLBI) observations, and temporal monitoring. To date, the discovery of 22 new class II methanol lines has been reported, including the detection of 15 torsionally excited lines (Breen et al. 2019; Brogan et al. 2019; MacLeod et al. 2019) and the first detection of isotopic methanol masers in three transitions (Chen et al. 2020b). This large variety of rare maser species detected during the flaring event was the motivation behind this search for ammonia lines towards G 358.931−0.030.

2 OBSERVATIONS AND DATA REDUCTION

We report on a series of observations, including both metastable and non-metastable ammonia transitions, targeting the 6.7-GHz methanol maser G 358.931−0.030 that was recently reported to be undergoing a period of flaring (Sugiyama et al. 2019). In addition to primary observations conducted with the Australia Telescope Compact Array (ATCA) and National Science Foundation's (NSF) Karl G. Jansky Very Large Array (VLA), further observations have also been conducted with the 65-m Tianma (TMRT) and the 26-m Hartebeesthoek radio telescopes. The TMRT notably made the first detection of the (6, 3) and (6, 5) masers on 2019 March 17 following the initial (7, 5) ammonia maser detection made with the ATCA on 2019 March 5. Together with several epochs of Hartebeesthoek observations, the TMRT observations are included here to provide an assessment of the temporal variability of the detected ammonia maser emission. Additionally, results from a Korean VLBI Network (KVN) fringe test are included, as the detected (6, 5) emission is useful for constraining the brightness temperature of the flaring component.

Observations of both metastable and non-metastable ammonia transitions were made across four epochs with the ATCA, and one with the NSF's Karl G. Jansky VLA. These observations included 15 ammonia transitions, together with one isotopic ammonia transition, which have rest frequencies between 18 and 26 GHz [specifically, ammonia (9, 6), (8, 5), (6, 3), (8, 6), (7, 5), (11, 9), (4, 1), (6, 5), (2, 1), (9, 8), (1, 1), (2, 2), (3, 3), (4, 4), (6, 6), and $^{15}NH_3$ (5, 5)]. Each of the transitions was observed at up to three epochs. All observations targeted the reported position of the 6.7-GHz methanol maser (J2000 position: $17^h43^m10\overset{s}{.}02$, $-29°51'45\overset{''}{.}8$; Caswell et al. 2010), which has since been slightly refined ($17^h43^m10\overset{s}{.}10$, $-29°51'45\overset{''}{.}5$; Breen et al. 2019). Table 1 summarizes the basic details of the observations, including telescope and array configuration, observation bandwidths and channel spacing, phase calibrator used, duration of the observations, and total integration time. Details of the observed lines, adopted rest frequencies, observed velocity coverage, velocity resolution, synthesized beam size, and RMS noise are given in Table 2.

2.1 Rest-frequency calculation

It is important to note that, for the detected ammonia maser transitions in this study, we adopted rest frequencies calculated as a weighted average over hyperfine components. The weights were the hyperfine line catalogue intensities. The hyperfine component frequencies and the catalogue intensities were taken from the VASTEL data base.[1] The rest frequencies we calculate for these lines are 19 757.579 MHz

[1] http://cassis.irap.omp.eu/?page = catalogs-vastel

Table 2. Target ammonia lines, followed by the adopted rest frequency (with errors in the last digit in parentheses) and observation epoch preceded by a letter indicating the array (A = ATCA, V = VLA), smoothed to the resolution shown. Detected transitions are marked with a leading '*'. Rest frequencies marked with a trailing '†', rather than numerical reference, are those from our calculations, which deviate from the previously reported values in the literature (see Section 2.1).

Spectral line	Rest freq. (MHz)	2019 Epoch (telescope DOY)	$V_{coverage}$ (km s^{-1})	$V_{res.}$ (km s^{-1})	Beam (arcsec × arcsec)	RMS (mJy)
NH_3 (9, 6)	18 499.390(5)[a]	A101	32	0.02	14.6 × 2.4	24.8
NH_3 (8, 5)	18 808.507(5)[b]	A096	39	0.02	27.1 × 21.2	31.5
		A101	31	0.02	14.3 × 23.3	33.6
*NH_3 (6, 3)	19 757.579(10)†	V094	60	0.12	1.62 × 0.26	80
		A096	30	0.02	26.0 × 20.5	38.9
NH_3 (8, 6)	20 719.221(10)[b]	A064	925	0.45	10.7 × 4.7	33.4
		A096	36	0.02	25.3 × 19.5	50.0
*NH_3 (7, 5)	20 804.830(5)[b]	A064	922	0.45	10.6 × 4.7	24.5
		A084	50	0.02	1.77 × 0.39	70.0
		V094	57	0.11	1.20 × 0.32	80
NH_3 (11, 9)	21 070.739(5)[c]	A064	910	0.44	10.5 × 4.6	27.3
NH_3 (4, 1)	21 134.311(5)[b]	A064	907	0.44	10.5 × 4.6	27.6
*NH_3 (6, 5)	22 732.425(4)†	V094	52	0.10	1.06 × 0.34	80
NH_3 (2, 1)	23 098.8190(1)[d]	A064	830	0.41	9.6 × 4.2	35.9
NH_3 (9, 8)	23 657.471(5)[d]	A096	31	0.02	22.1 × 17.1	49.7
NH_3 (4, 4)	24 139.4169(1)[e]	A096	31	0.1	22.7 × 16.8	3.1
NH_3 (6, 6)	25 056.025(5)[e]	A064	765	0.37	8.8 × 3.9	29.5

[a]Madden et al. (1986).
[b]Hermsen et al. (1988).
[c]Mauersberger et al. (1987).
[d]Moran et al. (1973).
[e]Barrett, Ho & Myers (1977).

(6, 3), 20 804.830 MHz (7, 5), and 22 732.425 MHz (6, 5). The calculated (6, 3) and (6, 5) rest frequencies are 0.041 MHz higher and 0.004 MHz lower, respectively, than those previously reported in the literature (Nystrom, Palmer & Zuckerman 1978; Hermsen et al. 1988), while the (7, 5) rest frequency is identical (Hermsen et al. 1988).

2.2 ATCA observations

Four epochs of ATCA observations were conducted between 2019 March 5 and April 11 (DOY 064, 084, 096 and 101) during allocations of maintenance and Director's time. A summary of the observation specifications is given in Table 1. Four different array configurations were used, and during March 5 only three of the antennas were available for science, as noted. The Compact Array Broadband Backend (Wilson et al. 2011) was configured in CFB 64M-32k on March 5 and CFB 1M-0.5k for the other epochs. The former provided 64-MHz spectral zoom bands, each with 2048 channels, whereas the latter provided a number of 1-MHz zoom bands, each with 2048 channels (which have been combined in order to provide adequate velocity coverage; indicated in column 4 of Table 2). Observations of the 6.7-GHz methanol maser target were interleaved with observations of a nearby phase calibrator (given in column 7 of Table 1) every ∼8–10 min. Pointing observations were made on the phase calibrator (B1741−312 or B1714−336) once per hour. At each of the four epochs, observations of PKS B1934−638 and PKS B1253−055 were made for primary flux density and bandpass calibration, respectively.

All data were reduced following the procedure outlined in Breen et al. (2019) and details of the velocity coverage, velocity resolution (sometimes after smoothing), synthesized beam, and RMS noise characteristics are given in Table 2. Well-calibrated, high-SNR, ATCA observations during good weather conditions have a nominal astrometric accuracy of approximately 0.5 arcsec (Caswell 1997).

2.3 VLA observations

VLA observations of the three NH_3 lines were made on 2019 April 4 (DOY 094) during a 1.5-h allocation of Director's Discretionary Time in B-array. Details of the observations are given in Table 1. Each of the observed lines (indicated in Table 2) was allocated a 4-MHz zoom band, each with dual polarization and 512 spectral channels. 3C286 was used to calibrate both the bandpass and primary flux density and observations of phase calibrator J1744−3116 were made throughout the observation. Astrometric uncertainty for our VLA B-array observations is approximately 30 milliarcsec.

Data were reduced by the VLA calibration pipeline using the Common Astronomy Software Applications package, applying standard techniques for the reduction of VLA spectral line data. The MIRIAD task *imfit* was then used to derive the maser spot distribution by fitting a two-dimensional (2D) Gaussian to the emission present in each channel map. This method allowed us to estimate both the position (with typical fitting errors of 0.01 arcsec) and the flux densities of the maser emission.

2.4 Shanghai 65-m Tianma Radio Telescope (TMRT) observations

Detections of the (6, 3), (7, 5), and (6, 5) ammonia transitions were made during TMRT observations conducted on 2019 March 17 (DOY 076). The observations used a cryogenically cooled *K*-band receiver and the digital backend system, allowing each line a 23.4-MHz spectral band, each with 4096 channels (corresponding to a velocity channel spacing of at least 0.09 km s^{-1}). Observations of the target were followed by reference observations with a 30-

Table 3. Properties of the ammonia masers detected towards G 358.931−0.030 derived from ATCA and VLA observations, including the measured peak positions, the minimum, maximum, and peak velocities, uncertainty in velocity (based on the uncertainty in the respective rest frequencies), the peak and integrated flux densities, and the maximum linear and circular polarization percentage (from ATCA observations only).

Ammonia transition	Epoch (DOY)	RA (2000) (^{h} ^{m} ^{s})	Dec. (2000) ($^{\circ}$ $'$ $''$)	V_{min}	V_{max}	V_{peak} (km s^{-1})	$V_{Uncert.}$	S_{peak} (Jy)	S_{int} (Jy km s^{-1})	Linear pol. percentage	Circular pol. percentage
(6, 3)	V094	17 43 10.101	−29 51 45.72	−17.8	−15.0	−15.4	(0.16)	9.5	7.1	–	–
	A096	17 43 10.08	−29 51 45.4	−17.8	−15.0	−15.5	–	14.1	7.9	1.5	<0.5
(7, 5)	A064	17 43 10.08	−29 51 45.8	−15.7	−14.9	−15.2	(0.07)	0.3	0.2	–	–
	A084	17 43 10.10	−29 51 45.8	−15.7	−15.0	−15.3	–	4.0	1.3	<2.0	<2.0
	V094	17 43 10.099	−29 51 45.71	−15.6	−15.0	−15.3	–	1.3	0.5	–	–
(6, 5)	V094	17 45 10.099	−29 51 45.71	−18.0	−14.7	−15.3	(0.06)	30.7	22.1	–	–

s integration time on each. The total on-source time was 22 min. The noise diode was used to carry out flux density calibration, and is expected to be accurate to $\lesssim$10 per cent. At the frequency of these observations, the TMRT has a beam size of ∼45 arcsec and an aperture efficiency of ∼50 per cent, corresponding to a sensitivity of 1.6 Jy K^{-1}. During the observations, the system temperature was between 100 and 150 K, resulting in a typical RMS noise of 0.15 Jy per spectral channel.

2.5 Hartebeesthoek observations

Monitoring observations of the (7, 5) and (6, 5) transitions were also conducted with the Hartebeesthoek radio telescope beginning on 2019 March 27 (DOY 086) and ending on 2019 April 3 (DOY 093) and 2019 August 3 (DOY 215) for the (7, 5) and (6, 5) transitions, respectively. The 1.3-cm receiver utilized for these observations is a cryogenically cooled, dual-polarization receiver. The point source sensitivity values for right circular and left circular polarization are 10.79 and 10.36 Jy K^{-1}, respectively. The velocity extent of the observations, for each of the observed transitions, is −46 to +12 km s^{-1} with a resolution of 0.1 km s^{-1} and a beam size of 2.2 arcmin. Flux density calibration of the Hartebeesthoek observations is expected to be accurate to $\lesssim$10 per cent.

2.6 Korean VLBI Network observations

Two hours of observing time were approved with the KVN in response to a request for Director's Discretionary Time for follow-up imaging of the maser flare event. Observations were conducted on 2019 March 25 (DOY 084) with three stations. Data were recorded at an 8-Gbps recording rate, providing 512-MHz bandwidth of left-hand circular polarized signal at each of the four simultaneously operating *K*, *Q*, *W*, and *D* frequency bands of the KVN, with 2-bit, Nyquist sampling. Data were correlated at the Korea Japan Correlation Center (Lee et al. 2015) with a frequency channel separation of 15.625 kHz, corresponding to 0.21 km s^{-1} velocity spacing. The resulting beam size for these KVN observations is 17.3 × 1.9 milliarcsec.

2-min scans of G358 were interspersed with 2-min scans of quasar J1744−3116 that was used for phase calibration and the observing session began and ended with scans on delay calibrators NRAO530 and BLLAC. Data were reduced using the Astronomical Image Processing Software (Greisen 2003) in which flux calibration was carried out using system noise measurements and gain characteristics of each of the three stations, providing a flux determination that is expected to be accurate to ∼10 per cent.

3 RESULTS

Observations of 15 ammonia transitions and one isotopic ammonia transition have resulted in the identification of a further rare site of ammonia maser emission detected in our Galaxy. In total, three ammonia maser lines were detected towards G 358.931−0.030; the (6, 3), (7, 5), and (6, 5) non-metastable transitions, the last one being the first unambiguous astronomical maser ever detected in that transition. The characteristics of each of the detections made with the ATCA and VLA are summarized in Table 3, including the fitted position of the maser peak emission as well as flux density and velocity information. Observations of the (6, 3) and (7, 5) transitions made with the ATCA include full polarization information and we find significant linearly polarized emission in the stronger (6, 3) transition but no significant circularly polarized emission (i.e. greater than 0.5 per cent of the Stokes I flux density). Higher sensitivity observations of the (7, 5) transition would be needed to confidently determine whether there are low levels (> 2 per cent of the Stokes I flux density) of linear or circular polarized emission.

Absolute positions of the detected ammonia masers (Table 3) confirm that they are associated with the target star formation region, which was displaying contemporaneous flaring in the 6.7-GHz class II methanol maser transition. A detailed maser spot map, showing the distribution of the respective maser lines, is given in Fig. 2. This figure shows that the peak emission (at the least negative velocities) in each of the transitions is located to the east of the continuum source, while the bulk of the additional (6, 3) and (6, 5) emission is more widely distributed, mostly to the north.

Ammonia (6, 5) was detected in the autocorrelation and cross-correlation KVN data, and while the total integration time was not sufficient to conduct accurate astrometry, the KVN was able to produce an image of the emission at milliarcsecond resolution (Fig. 3) in order to help constrain brightness temperatures. The image shows compact, unresolved maser emission with an integral flux of 2.12 ± 0.41 Jy emitting from a region with a deconvolved angular full width half-maximum size of 17 × 3 milliarcsec, determined by a 2D Gaussian fit to the VLBI image. The 2.38 ± 0.25 Jy beam^{-1} flux density of the maser corresponded to a >9σ detection against the 0.253 Jy beam^{-1} RMS noise of the processed VLBI image.

Spectra for each of the maser detections are given in Fig. 1 and include a number of observation epochs. In the case of the (6, 3) maser transition, the linearly polarized emission (scaled by a factor of 10) detected with the ATCA on DOY096 is shown in addition to the Stokes I emission. Despite the relatively large velocity uncertainty (related to the uncertainty in the line rest frequency; listed in Table 3 and shown in Fig. 1), all of the ammonia maser features are contained

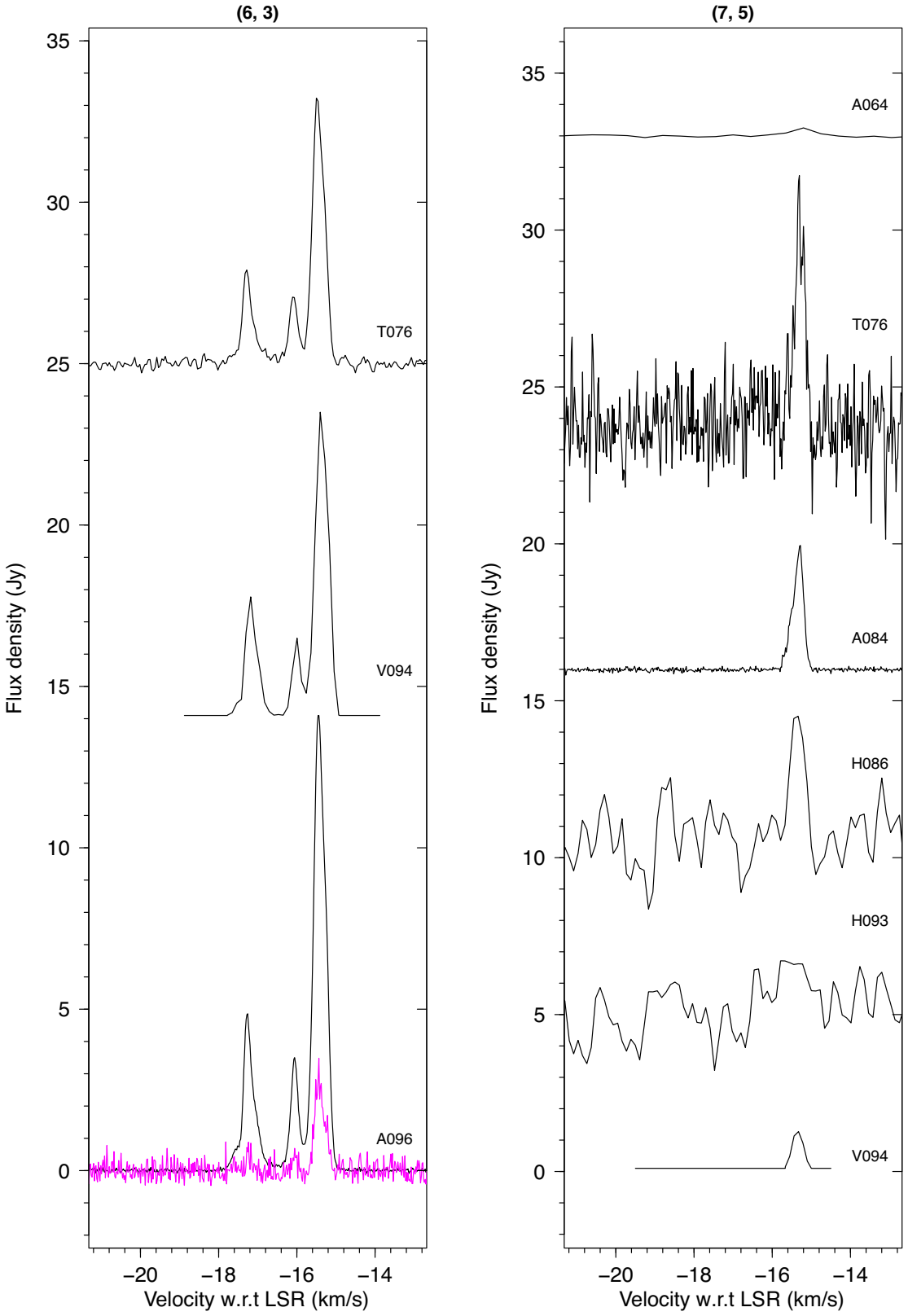

Figure 1. Ammonia (6, 3), (7, 5), and (6, 5) maser spectra. The telescope used (A: ATCA; V: VLA; T: TMRT; H: Hartebeesthoek) and DOY of the observation are indicated to the right of each spectrum. Black lines indicate Stokes I and magenta shows the detected linearly polarized emission scaled by 10.

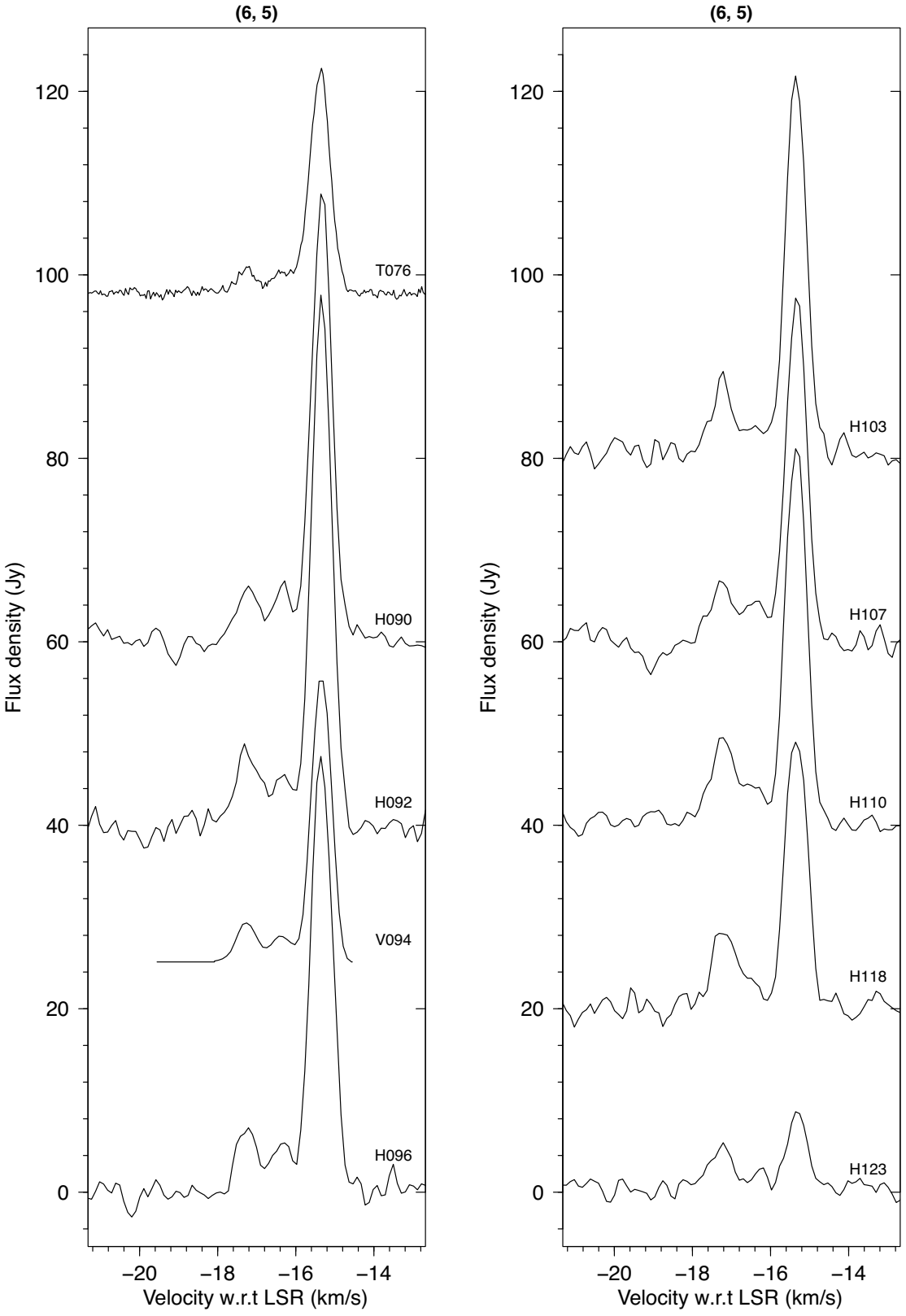

Figure 1. *Continued.*

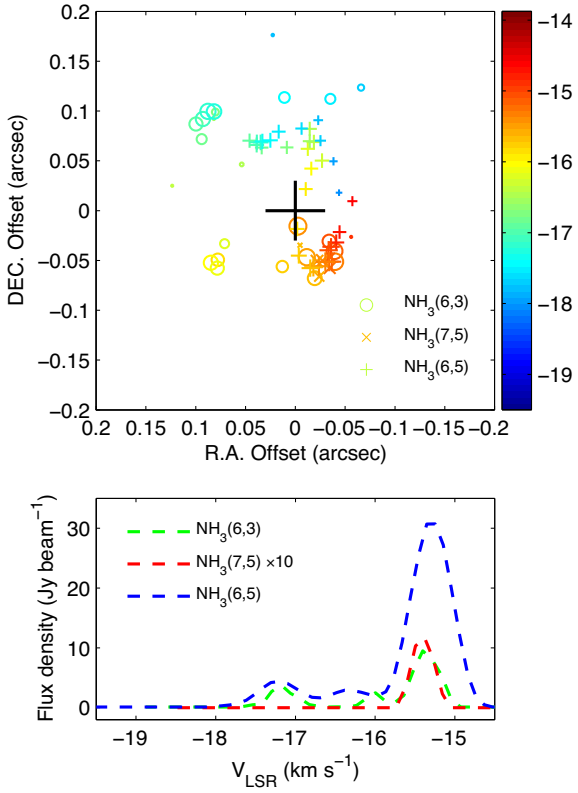

Figure 2. VLA ammonia (6, 3), (7, 5), and (6, 5) maser spot distribution relative to the ALMA continuum source MM1 (J2000 position: α = 17:43:10.1015, δ = −29:51:45.6936) marked by a black cross. The extent of the black cross shows the absolute positional uncertainty of 0.03 arcsec, while the extent of the coloured symbols indicates the positional uncertainty in the individual maser spot.

within the velocity range of the target 6.7-GHz methanol maser (−19.6 to −12.7 km s^{-1}; Breen et al. 2019).

Significant changes in the detected spectral profiles are seen (Fig. 1) across the observation epochs for all three ammonia transitions. The first ammonia maser detection was made on DOY064 in the (7, 5) transition, just 50 d after the 6.7-GHz methanol maser was reported to be undergoing flaring activity (Sugiyama et al. 2019). The peak flux density of the 6.7-GHz methanol maser on DOY065 was 981 Jy (Breen et al. 2019). Our observations indicate that the period of ammonia maser emission is likely to have been a short, transient phenomenon, closely linked to the 6.7-GHz methanol maser flaring activity, with both the (7, 5) and (6, 5) transitions appearing to wane significantly, first in the (7, 5) transition. Though outside the range of Fig. 1, further monitoring from Hartebeesthoek finds that the (6, 5) transition is detectable up until DOY133, with no detection of the emission in the following epoch on DOY139.

In addition to these maser lines, we have detected thermal emission in the (1, 1), (2, 2), and (3, 3) metastable transitions of ammonia.

4 DISCUSSION

To date, ammonia masers have only been detected towards approximately a dozen sites within the Galaxy [e.g. W33, DR 21(OH), W51-IRS2, W49, NGC 7538, NGC 6334I, SgrB2, IRAS20126+4104, G 5.89−0.39, G 23.33−0.30, and G 19.61−0.23; Wilson et al. 1982; Guilloteau et al. 1983; Madden et al. 1986; Hofner et al. 1994; Zhang et al. 1999; Walsh et al. 2007, 2011; Hunter et al. 2008; Mills et al. 2018]. While the observations of these sources are not homogeneous, both in lines targeted and sensitivity, the detected maser transitions vary widely. In addition to the inconsistencies in the presence or absence of the various ammonia maser transitions, the relative strengths of the detected transitions appear to be highly source dependent. Even so, the set of ammonia masers we detect towards G 358.931−0.030 appears to show some further deviations from what little commonality can be found across the known sample. Typically, in sources with multiple detected ammonia maser lines, the (9, 6) transition is observed to be the brightest (e.g. Hoffman & Joyce 2014; Mei et al. 2020), yet we do not detect this line towards G 358.931−0.030. However, this difference between the maser line ratios, when comparing G 358.931−0.03 to the previously known sample, is not necessarily surprising as this is the first flaring source towards which ammonia masers have been detected.

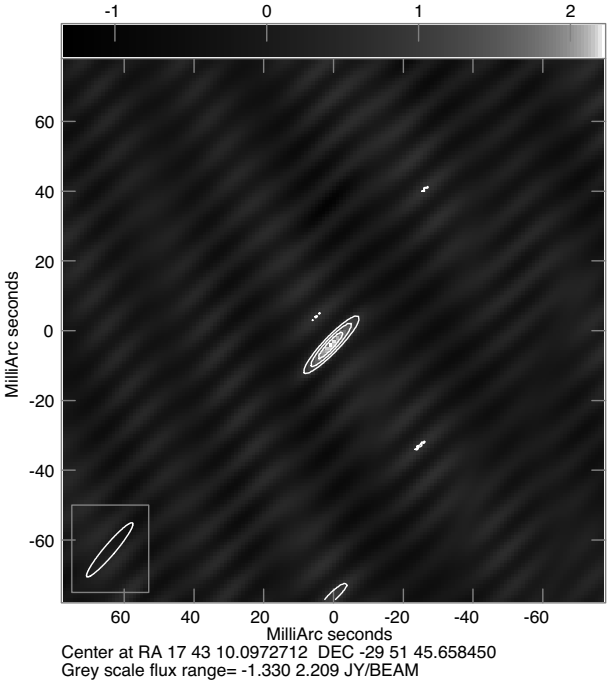

Figure 3. Field image of the NH_3 (6, 5) emission as detected during the KVN fringe test. Flux densities are shown in grey scale and contours mark the 3σ, 5σ, 7σ, and 9σ levels (σ = 0.26 Jy per beam). The synthesized beam shape for the experiment is shown in the plot (bottom left).

4.1 Ammonia (6, 5) maser emission

Mauersberger, Wilson & Henkel (1988) reported the possible detection of a weak (6, 5) maser in an extensive ammonia study towards W3(OH). They argued the maser nature of the transition based on its strength [more than twice as bright as the (5, 4) or (7, 6) lines they detected] and a peak velocity redshifted by 0.5 km s^{-1} with respect to the detected absorption, concluding that it was probably amplifying the continuum emission. Other past observations of the ammonia (6, 5) transition have not found any maser emission; e.g. Henkel et al. (2013) found no emission towards the most prominent ammonia maser site, W51.

The (6, 5) emission we report here shows both a narrow spectral line width (comparable to other examples of ammonia masers), co-located with other masing species, and significant variability in the peak emission component. The level of variability alone (further discussed in Section 4.2) implies a brightness temperature of the

order of 10^5 K, while the detection of the primary (6, 5) emission in our KVN fringe test implies a brightness temperature of $>10^8$ K. These factors leave little doubt that the (6, 5) emission we report here is the result of a maser process, making this the first unambiguous detection of astronomical ammonia (6, 5) masers.

4.2 Maser variability

To date, variability in ammonia masers has only been identified from two sources, W51 (Wilson & Henkel 1988) and SgrB2 (Mei et al. 2020). Wilson & Henkel (1988) observe variability from numerous non-metastable ammonia lines towards W51d and W51-IRS1 over a period of approximately 3 yr. Observations by Mei et al. (2020) reveal a rich maser environment towards SgrB2, with masers from numerous non-metastable ammonia transitions that were not detected in previous observations of the source.

Towards G 358.931−0.030, we observe variability in all three of the detected ammonia lines. During this same time period, flaring was detected in class II methanol maser lines, driven by a massive young stellar object accretion burst event (Burns et al. 2020; Stecklum et al. 2021). In the case of the (6, 3) and (6, 5) emission, where multiple components are detected, we see flaring predominantly constrained to the peak emission component, which in both cases are located closest to the continuum source and at higher velocity values.

Upper limits for the minimum variability time-scales, defined as the time taken for a 50 per cent change in peak flux density to occur, are 26 and 12 d for the (6, 5) and (7, 5) lines, respectively. These time-scales correspond to linear scales of 0.022 and 0.010 pc and subsequently angular scales (at a distance of 6.75 kpc; Brogan et al. 2019) of 0.67 and 0.3 arcsec for the (6, 5) and (7, 5) masing regions, respectively. These angular scales imply peak brightness temperatures for both maser lines of $>3 \times 10^5$ K.

4.3 Ammonia maser environment

The peak emission from all three ammonia transitions is clustered ∼0.02 arcsec south-west of the Atacama Large Millimeter/submillimeter Array (ALMA) continuum source (see Fig. 2) and covering a velocity range of −14.5 to −16.5 km s^{-1}. Contemporaneously, at this same south-west location and velocity range, strong (and variable) emission from the 21.981-GHz ($1_{0,1} \rightarrow 0_{0,0}$, $F = 2$–1) HNCO and 20.460-GHz ($3_{2,1} \rightarrow 4_{1,4}$) HDO is detected by Chen et al. (2020a). Their observations reveal that this south-west region is also free of water masers, which are located at more extreme negative velocities, to the north of the MM1 continuum source.

Broadly, the maser emission from all three ammonia transitions follows the same spatial distribution and velocity structure as observed from the 21.981-GHz HNCO, 20.460-GHz HDO ($3_{2,1} \rightarrow 4_{1,4}$), and isotopic methanol ($^{13}CH_3OH$) masers by Chen et al. (2020a) during this same time period (early April 2019). Chen et al. identify that these masers appear to be tracing a two-arm accretion flow about the high-mass young stellar object. Of the three ammonia maser transitions we observe towards G 358.931−0.030, the (6, 3) transition, which covers both the widest velocity range and angular scale, appears to most accurately follow the suggested two-arm spiral model presented by Chen et al. (2020a). Burns et al. (2020) present VLBI observations of the 6.7-GHz class II methanol masers during the flare event. Their observations describe a thermal radiation heat-wave emanating from the accretion source, and by their second epoch on 2019 February 28, the class II maser emission is observed further out from the protostar than the ammonia masers we report here.

4.4 Pumping model calculations

In Fig. 2, it can be seen that that the brightest maser emission in NH_3 transitions (6, 3), (7, 5), and (6, 5) is formed in a region located closer than 0.05 arcsec south-west of the MM1 source. In the same region, the emission of bright methanol masers at frequencies of 6.67, 12.18, and 23.12 GHz is observed (Bayandina et al. 2022), as well as the emission of ^{13}CH3OH, HDO, and HNCO masers (Chen et al. 2020b). These masers are formed in conditions characterized by a relatively large difference between the temperatures of dust and gas, which may arise due to the flare nature of accretion on to a young star formed in G 358.931−0.030 (Chen et al. 2020a). One can assume that the observed NH_3 masers form in similar conditions. Indeed, pumping models of Brown & Cragg (1991) show that the NH_3 (6,3) transition can be inverted at high colour temperatures of the infrared emission. The emission in the NH_3 (6, 5) line is also present in the region 0.1–0.15 arcsec north of the MM1 source, where there is no methanol maser emission at 6.67 GHz; however, there are methanol masers at 12.18 GHz and from the highly excited, and recently discovered, methanol maser lines at 12.23 and 20.97 GHz (Bayandina et al. 2022). This suggests that the maser emission in the newly detected NH_3 (6, 5) line can be excited by infrared emission with a high colour temperature exceeding 100 K. In order to test this hypothesis and interpret the observations, we used radiative transfer calculations.

Radiative transfer calculations were performed using the large velocity gradient (LVG) approximation with custom code (https://github.com/ParfenovS/LVG_LRT). The NH_3 energy levels and radiative transition sets[2] were similar to those used by Schmidt et al. (2016). We extended the molecular data from the Jet Propulsion Laboratory (JPL) database (Pickett et al. 2010) with the data from the CoYuTe list (Coles, Yurchenko & Tennyson 2019) that includes the energy levels for the excited vibrational states. The resulting NH_3 model consists of the levels with $J < 16$ of the ground state and symmetric bend vibrational mode $\nu_2 = 1$. The total number of energy levels and transitions was 340 and 5498 for p-NH_3 and 172 and 1477 for o-NH_3, respectively. The collisional rates were taken from Danby et al. (1988) and extrapolated for the transitions absent in their data using the method of Brown & Cragg (1991) with the difference that we did not omit the transitions involving the ground state when fitting the extrapolation formulae. Brown & Cragg (1991) suggested that the probability of transitions between vibrationally excited and ground states is likely significantly smaller than transitions within a vibrational state. Following Brown & Cragg (1991), the extrapolated collisional rates for transitions involving a vibrational quantum number change were additionally scaled down by a factor of 1000.

The basic model parameters are specific column density of NH_3 ($N/\Delta V$), gas density (n_{H_2}) and temperature (T_{gas}), background emission, parameters of external dust and dust within the masering region (internal dust), and beaming factor ϵ^{-1} (defined as the ratio of the radial to tangential optical depths representing the elongation of the maser region along the line of sight; see e.g. Cragg, Sobolev & Godfrey 2005). The internal and external dust parameters include the dust temperature, optical depth, and dust mass absorption coefficients. The latter were taken from Robitaille (2017) and were the same as those used by Stecklum et al. (2021) to model the spectral energy distribution of the MM1 source. In addition, the external dust emission is characterized by the dilution factor, W_d. Given the observed close association between NH_3 and CH_3OH masers, the

[2]The molecular data in LAMDA format used in this study can be found at https://github.com/ParfenovS/Spectroscopy/tree/main/NH3.

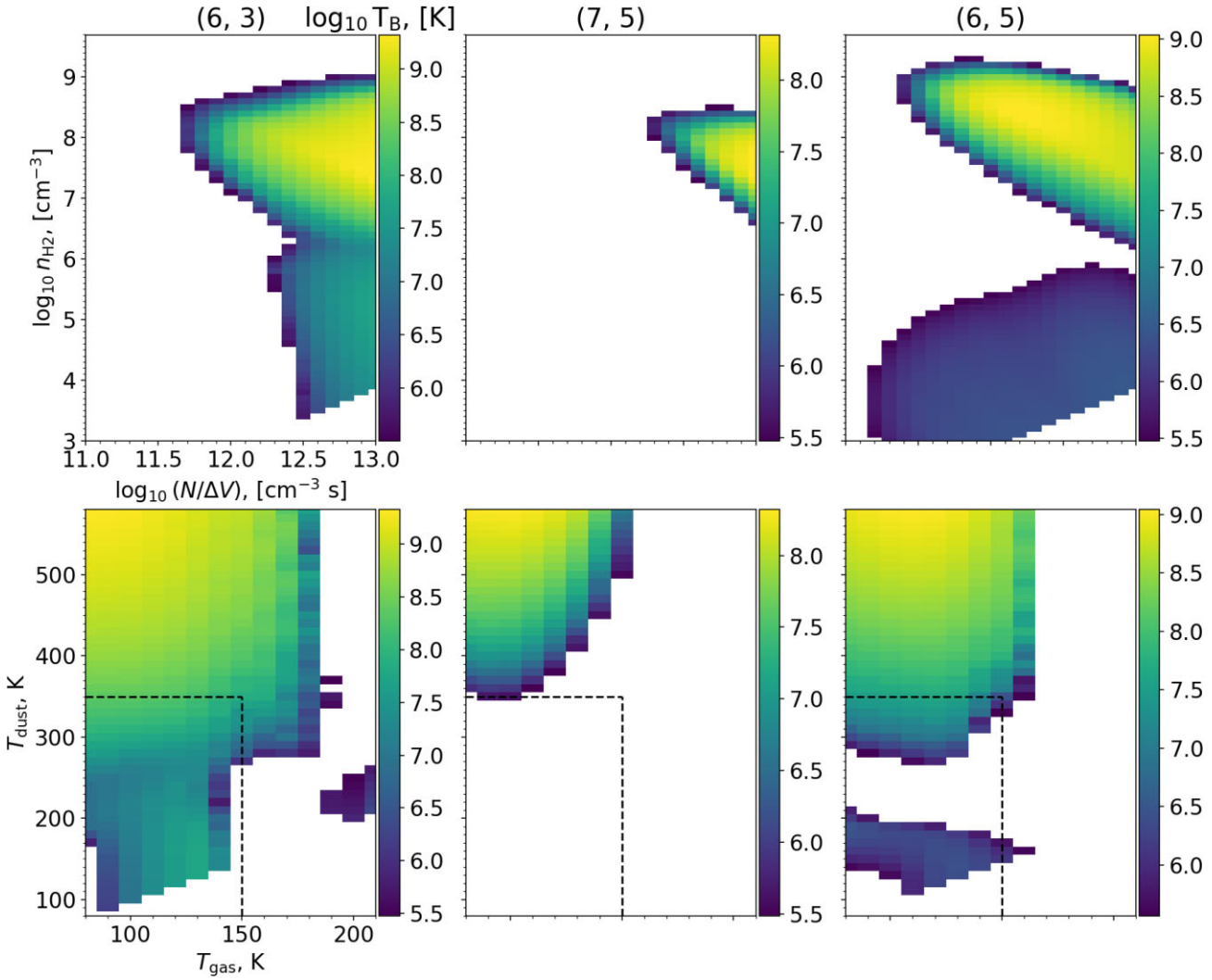

Figure 4. Maximum brightness temperatures of the (6, 3) (left-hand panels), (7, 5) (middle panels), and (6, 5) (right-hand panels) transitions of NH_3. Lower panels show maximum brightness temperatures over the whole range of $N/\Delta V$ and n_{H_2} for the fixed values of T_{dust} and T_{gas}. Upper panels show maximum brightness temperatures over the whole range of T_{dust} and T_{gas} for the fixed values of $N/\Delta V$ and n_{H_2}. Blank areas correspond to the case when the model brightness temperatures in a given transition are lower than 3×10^5 K or when the optical depth in the (1,1), (2, 2), or (3, 3) transition is lower than -1. Black dashed lines in lower panels denote the temperature region discussed in Section 4.4 in relation to the conditions where only the (6, 3) maser forms.

external dust optical depth of 1 at 10^4 GHz and $W_d = 0.5$ were the same as in the class II methanol maser calculations of Cragg et al. (2005). The external dust temperature, T_{dust}, was independent of the internal dust temperature. We set the upper limit of 580 K for the external dust temperature that is close to the maximum dust temperatures in the model of Stecklum et al. (2021). The internal dust temperature was equal to T_{gas}. Hereafter, dust temperature references the external dust temperature, T_{dust}. The internal dust optical depth was calculated assuming the gas-to-dust mass ratio obtained with equations (21) and (22) from Kuiper et al. (2010) and an initial gas-to-dust mass ratio of 38 (Giannetti et al. 2017; Stecklum et al. 2021), a mean molecular weight per H_2 molecule of 2.8, a maser line width of 0.5 km s^{-1}, and the NH_3 abundance (with respect to H_2) of 5×10^{-6} that is similar to that estimated for SgrB2 by Mei et al. (2020). The background emission was the cosmic microwave background with a temperature of 2.7 K. The specific column density in LVG approximation is defined along the direction perpendicular to the line of sight. To estimate the upper limit for NH_3 specific column density corresponding to the brightest masers, we assume that the maser cloud has an angular size of 10 milliarcsec, which is an average of the maximum and minimum angular sizes of 17×3 milliarcsec determined from the KVN data for the (6, 5) emission (see Section 3). This angular size corresponds to 68 au at a distance of 6.75 kpc. Our calculations, presented below, show that the brightest masers in the (6, 5) transition occur at $n_{H_2} \sim 10^8$ cm^{-3}. With this gas density, along with the maser cloud size, maser line width, and NH_3 abundance that are given above, we obtain the upper limit for NH_3 specific column density of 10^{13} cm^{-3} s. This upper limit defines the extent for the models' grid calculated below. The brightness temperature, T_B, in the (6, 5) transition becomes higher than 10^8 K for $\epsilon^{-1} \geq 2$ in the models with maximum considered T_{dust}. For the calculations presented below, we fixed the value of $\epsilon^{-1} = 5$ at which $T_B > 10^8$ K for a wide range of parameters and at which the maximum T_B for the (6, 5) line is 10^9 K.

The grid of models was calculated for different values of $N/\Delta V$, n_{H_2}, T_{gas}, and T_{dust}. From the grid, we then formed the subset of models where there is no significant maser effect, i.e. the optical depth exceeds -1, in the (1, 1), (2, 2), and (3, 3) transitions in which

we detected the thermal emission. We used only this subset for further interpretation of our observations. From this subset, we selected, for each of the detected NH_3 maser transitions, those models where T_B is higher than the limit of 3×10^5 K (see Section 4.2). In Fig. 4, it is seen that the model brightness temperatures are consistent with the limit under the conditions with gas densities $<10^9$ cm^{-3}, gas temperatures of <200 K, and dust temperatures of >80 K. Similar to the HDO and HNCO masers, the NH_3 maser brightness is consistent with observations when $T_{dust} \geq T_{gas}$.

To interpret the emission in the (6, 3) line detected farther than 0.05 arcsec from the MM1 source, where the emission in the (7, 5) and (6, 5) lines is absent, we selected the models for which T_B in the (6, 3) transition is higher than 3×10^5 K, and T_B in the (7, 5) and (6, 5) lines is lower than 455 and 381 K, respectively. These upper limits for the (7, 5) and (6, 5) transitions are obtained from equation (1) in Chipman et al. (2016) assuming that the maser region angular size does not exceed 0.67 arcsec (see Section 4.2) and using 3σ detection limit of about 50 mJy per beam for the VLA data. Our models show that the (6, 3) emission observed farther than 0.05 arcsec from MM1 forms at relatively low dust and gas temperatures of $T_{dust} < 350$ K and $T_{gas} < 150$ K (see dashed lines in Fig. 4), respectively, relatively high specific column densities of $>10^{12}$ cm^{-3} s, and in the density range of $n_{H_2} = 10^4$–10^9 cm^{-3}. These conditions are within those suitable for the CH_3OH maser formation at the outer disc regions in the model of Stecklum et al. (2021). Bayandina et al. (2022) show that the CH_3OH masers trace a two-arm spiral pattern that is more extended from the MM1 on 2019 June 4 than on 2019 February 25. There are no data on the CH_3OH maser distribution in epoch V094 (2019 April 4). Given that the (6, 3) maser can form in the conditions suitable for CH_3OH maser excitation, we suggest that the (6, 3) masers detected farther than 0.05 arcsec from the MM1 source in epoch V094 trace the extent of CH_3OH maser spiral pattern in this epoch. Note that the temperature range of $T_{dust} < 350$ K and $T_{gas} < 150$ K also includes the temperature range of $T_{dust} = 100$–220 K and $T_{gas} < 350$ K where the (6, 5) maser forms. However, these temperature ranges do not exclude each other when one considers the conditions for which only (6, 3) or only (6, 5) maser forms. There is a large set of models with temperatures suitable for excitation of both the (6, 3) and (6, 5) masers but with the values of n_{H_2} and $N/\Delta V$ so that only one of the two masers is excited. For $T_{dust} < 220$ K, the (6, 5) maser forms under typically lower gas densities $n_{H_2} < 10^6$ cm^{-3} than the (6, 3) maser.

The brightness temperature in the (7, 5) and (6, 3) lines is lower than the VLA detection limits of 455 and 505 K, respectively, corresponding to the detection limit of 50 mJy per beam, in the region 0.1–0.15 arcsec north of the MM1 source where only the (6, 5) maser emission is detected in the VLA data. According to our calculations, this emission arises at $T_{dust} = 100$–200 K, $T_{gas} < 160$ K, and $n_{H_2} < 10^6$ cm^{-3}. The model of Stecklum et al. (2021) shows that such gas densities are consistent with the upper layers of disc where the conditions also favour the formation of class II methanol masers. This explains the observed close association between the class II methanol masers and NH_3 masers in the (6, 5) transition.

The brightness temperature in the (6, 5) line exceeds the limit of 10^8 K estimated with KVN in 2019 March for $T_{dust} > 380$ K. In the model of Stecklum et al. (2021) for the burst epoch that is used to describe the infrared data for G 358.931−0.030 in 2019 March, such dust temperatures are achieved at a distance of $\lesssim$400 au from the protostar. Therefore, the brightest maser detected with KVN in the (6, 5) transition originates in a close proximity to the protostar and is pumped by emission from hot dust. Our calculations, thus, confirm our initial hypothesis that the newly detected NH_3 (6, 5) maser line can be excited by infrared emission from dust with temperatures exceeding 100 K.

Additional constraints for the physical conditions can be inferred from the observations in epochs A064 and A096. In epoch A064, the maser emission in the (7, 5) line was observed, while there was no detection in the (8, 6), (11, 9), (4, 1), (2, 1), and (6, 6) lines. In epoch A096, the maser emission in the (6, 3) and (6, 5) lines was detected and the emission in the (8, 5), (8, 6), (9, 8), and (4, 4) lines has not been detected. We assume that the maser emission detected in these two epochs has $T_B > 10^5$ K, and estimate the upper limits for T_B in non-detected lines with the RMS noise in Table 1 multiplied by 5.

Our models show that the (7, 5) maser in epoch A064 forms under the following conditions: $N/\Delta V > 10^{12.7}$ cm^{-3} s, $T_{dust} > 470$ K, $T_{gas} = 120$–140 K, and $n_{H_2} \sim 10^8$ cm^{-3}, which is consistent with its proximity to MM1, as observed in epoch V094. We therefore conclude that the (7, 5) maser spots have not moved significantly relative to the MM1 source in the time period between A064 and V094 epochs, which is in contrast to what has been observed from some CH_3OH maser spots (Bayandina et al. 2022). It is likely that the heatwave did not result in the dust temperature increase enough to excite these masers at farther distances from the MM1 source.

With the data on non-detected lines in epoch A096, one can place the limit of $T_{gas} < 110$ K and $N/\Delta V > 10^{11.6}$ cm^{-3} s for the (6, 5) maser formation at $T_{dust} > 250$ K. There are no additional constraints for the (6, 5) maser formation at $T_{dust} < 250$ K when taking into account the data from non-detected lines.

The data on non-detected lines in epoch A096 allow one to strengthen the limits on the conditions of the (6, 3) maser formation. Our calculations show that these masers form at $T_{gas} < 140$ K and $N/\Delta V > 10^{12}$ cm^{-3} s. There are no significant qualitative differences between the (6, 3) maser spectra in V094 and A096 epochs (see Fig. 1); thus, there are no signatures of significant changes of excitation conditions between epochs V094 and A096. Therefore, the limits obtained in epoch A096 can be applied to interpret the observations in epoch V094.

As seen in Fig. 4, T_B in the (6, 3) transition increases, in general, with increasing dust temperature in accordance to the results of Brown & Cragg (1991). Our calculations show that T_B in the (7, 5) and (6, 5) lines also increases with the dust temperature. Note, however, that the exact dependence of T_B on the dust temperature changes as the other parameters change. For example, as seen in Fig. 5, the brightness temperature in the (6, 5) line is more sensitive to the dust temperature changes in the range of $T_{dust} = 350$–400 K for the case where $T_{gas} = 80$ K compared to when $T_{gas} = 120$ K. Taking into account that the dust temperature varies with time, such a difference in the sensitivity to T_{dust} variations can be the reason for a different behaviour with time of different spectral components in the (6, 5) maser spectra shown in Fig. 1. From Fig. 5, it also follows that the brightness of the (7, 5) maser should decrease earlier than those for the (6, 3) and (6, 5) masers as the dust temperature decreases after the burst. The brightness of the (6, 5) maser should decrease earlier than that of (6, 3) maser. Data from other NH_3 transitions, covering a similar length period after the flare event as the (6, 5) line in this study, could be a good test of the NH_3 maser excitation model.

5 SUMMARY

We report the results of an ammonia line search and monitoring observations towards the flaring star formation region G 358.931−0.030 with the ATCA, VLA, TMRT, Hartebeesthoek, and KVN. We report the first unambiguous maser detection of the non-metastable ammonia (6, 5) transition in the Milky Way, along with detection

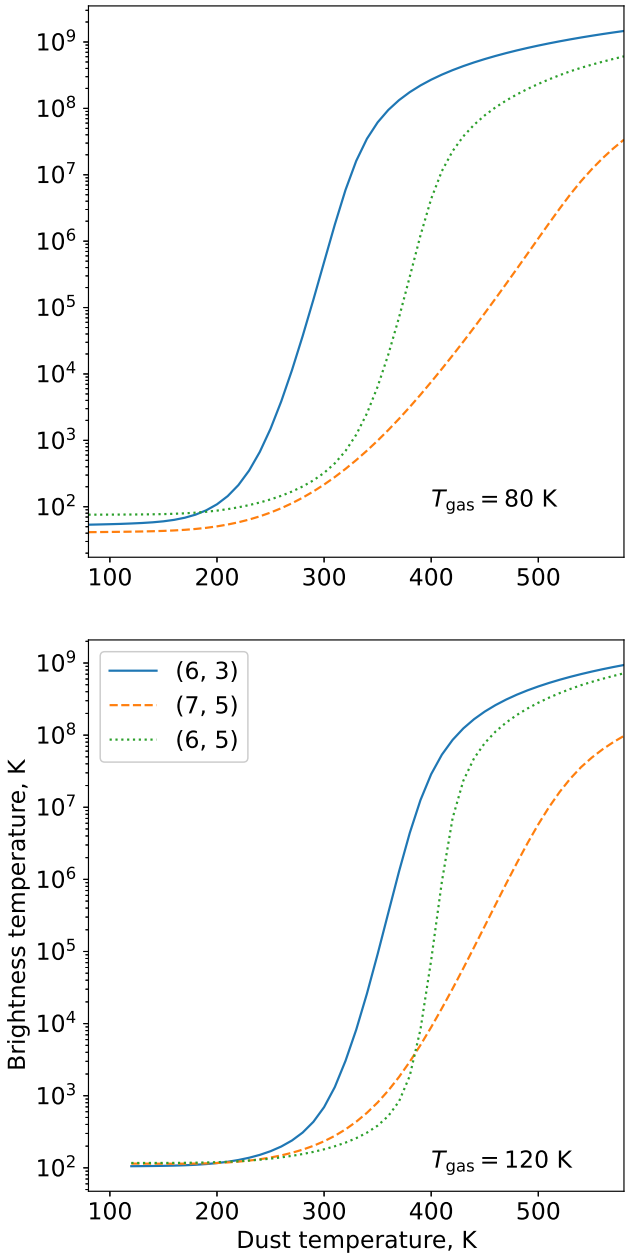

Figure 5. Dependence of the brightness temperature in different NH_3 transitions on the dust temperature for $N/\Delta V = 10^{12.8}$ cm^{-3} s, $n_{H_2} \sim 10^8$ cm^{-3}, $T_{gas} = 80$ K (upper panel), and $T_{gas} = 120$ K (lower panel).

and monitoring of the (7, 5) and (6, 3) ammonia maser lines. We observe the ammonia maser flaring during this accretion burst period of G 358.931−0.030. The distribution of these ammonia masers appears to be broadly consistent with the two-arm spiral accretion flow first discovered by Chen et al. (2020a). From the monitoring observations, significant variability is detected from the (6, 5) and (7, 5) lines during this flare period with variability time-scales of 26 and 12 d, respectively.

We use our observational data, including the high-resolution VLBI detection of the ammonia (6, 5) emission, as constraints for radiative transfer calculations that allow us to understand and investigate the pumping environment of these ammonia masers, along with other maser species that are spatially coincident. The results of these pumping model calculations support our hypothesis that the maser emission from the (6, 5) transition is excited by high colour temperature infrared emission (>100 K). Additionally, the line ratio between the (6, 5) and (7, 5) masers implies a dust temperature in excess of 400 K at the location of peak (6, 5) emission.

We determine, based on weighted averages of the hyperfine component frequencies, new rest frequencies for the ammonia (6, 3) and (6, 5) transitions. Our calculated values of 19 757.579 MHz for the (6, 3) transition and 22 732.425 MHz for the (6, 5) transition differ from those previously reported in the literature by +0.041 and −0.004 MHz, respectively.

ACKNOWLEDGEMENTS

We thank the anonymous referee for their useful comments that improved this manuscript. The ATCA is part of the Australia Telescope National Facility. This research has made use of NASA's Astrophysics Data System Abstract Service. SPE acknowledges the support of ARC Discovery Project (project number DP180101061). SSP and AMS were supported by the Ministry of Science and Higher Education of the Russian Federation (state contract FEUZ-2023-0019).

DATA AVAILABILITY

The data underlying this article will be shared on reasonable request to the corresponding author. ATCA data are open access 18 months after the date of observation and can be accessed using the Australia Telescope Online Archive (https://atoa.atnf.csiro.au).

REFERENCES

Barrett A. H., Ho P. T. P., Myers P. C., 1977, ApJ, 211, L39
Bayandina O. S. et al., 2022, AJ, 163, 83
Beuther H., Walsh A. J., Thorwirth S., Zhang Q., Hunter T. R., Megeath S. T., Menten K. M., 2007, A&A, 466, 989
Breen S. L., Sobolev A. M., Kaczmarek J. F., Ellingsen S. P., McCarthy T. P., Voronkov M. A., 2019, ApJ, 876, L25
Brogan C. L. et al., 2019, ApJ, 881, L39
Brown R. D., Cragg D. M., 1991, ApJ, 378, 445
Burns R. A. et al., 2020, Nat. Astron., 4, 506
Caswell J. L., 1997, MNRAS, 289, 203
Caswell J. L. et al., 2010, MNRAS, 404, 1029
Chen X. et al., 2020a, Nat. Astron., 4, 1170
Chen X. et al., 2020b, ApJ, 890, L22
Chipman A., Ellingsen S. P., Sobolev A. M., Cragg D. M., 2016, PASA, 33, e056
Coles P. A., Yurchenko S. N., Tennyson J., 2019, MNRAS, 490, 4638
Cragg D. M., Sobolev A. M., Godfrey P. D., 2005, MNRAS, 360, 533
Danby G., Flower D. R., Valiron P., Schilke P., Walmsley C. M., 1988, MNRAS, 235, 229
Giannetti A. et al., 2017, A&A, 606, L12
Greisen E. W., 2003, in Heck A., ed., Astrophysics and Space Science Library, Vol. 285, Information Handling in Astronomy – Historical Vistas. Springer-Verlag, Berlin, p. 109
Guilloteau S., Wilson T. L., Martin R. N., Batria W., Pauls T. A., 1983, A&A, 124, 322
Henkel C., Wilson T. L., Asiri H., Mauersberger R., 2013, A&A, 549, A90
Hermsen W., Wilson T. L., Walmsley C. M., Henkel C., 1988, A&A, 201, 285
Hoffman I. M., 2012, ApJ, 759, 76
Hoffman I. M., Joyce S. A., 2014, ApJ, 782, 83
Hoffman I. M., Seojin Kim S., 2011a, ApJ, 739, L15
Hoffman I. M., Seojin Kim S., 2011b, AJ, 142, 202
Hofner P., Kurtz S., Churchwell E., Walmsley C. M., Cesaroni R., 1994, ApJ, 429, L85

Hunter T. R., Brogan C. L., Indebetouw R., Cyganowski C. J., 2008, ApJ, 680, 1271
Johnston K. J., Stolovy S. R., Wilson T. L., Henkel C., Mauersberger R., 1989, ApJ, 343, L41
Kraemer K. E., Jackson J. M., 1995, ApJ, 439, L9
Kuiper R., Klahr H., Beuther H., Henning T., 2010, ApJ, 722, 1556
Lee S.-S. et al., 2015, J. Korean Astron. Soc., 48, 125
MacLeod G. C. et al., 2019, MNRAS, 489, 3981
Madden S. C., Irvine W. M., Matthews H. E., Brown R. D., Godfrey P. D., 1986, ApJ, 300, L79
Mangum J. G., Wootten A., 1994, ApJ, 428, L33
Mauersberger R., Wilson T. L., Henkel C., 1986, A&A, 160, L13
Mauersberger R., Henkel C., Wilson T. L., 1987, A&A, 173, 352
Mauersberger R., Wilson T. L., Henkel C., 1988, A&A, 201, 123
Mei Y., Chen X., Shen Z.-Q., Li B., 2020, ApJ, 898, 157
Mills E. A. C. et al., 2018, ApJ, 869, L14
Moran J. M. et al., 1973, ApJ, 185, 535
Nystrom H. J., Palmer P., Zuckerman B., 1978, Bull. Am. Astron. Soc., 10, 393
Pickett H. M., Poynter I. R. L., Cohen E. A., Delitsky M. L., Pearson J. C., Muller H. S. P., 2010, J. Quant. Spectrosc. Radiat. Transfer, 111, 1617
Robitaille T. P., 2017, A&A, 600, A11
Schilke P., Walmsley C. M., Mauersberger R., 1991, A&A, 247, 516
Schmidt M. R. et al., 2016, A&A, 592, A131
Stecklum B. et al., 2021, A&A, 646, A161
Sugiyama K., Saito Y., Yonekura Y., Momose M., 2019, Astron. Telegram, 12446, 1
Walsh A. J., Longmore S. N., Thorwirth S., Urquhart J. S., Purcell C. R., 2007, MNRAS, 382, L35
Walsh A. J. et al., 2011, MNRAS, 416, 1764
Wilson T. L., Henkel C., 1988, A&A, 206, L26
Wilson T. L., Batrla W., Pauls T. A., 1982, A&A, 110, L20
Wilson W. E. et al., 2011, MNRAS, 416, 832
Zhang Q., Ho P. T. P., 1995, ApJ, 450, L63
Zhang Q., Hunter T. R., Sridharan T. K., Cesaroni R., 1999, ApJ, 527, L117

This paper has been typeset from a TEX/LATEX file prepared by the author.